

# An RTK-SLAM Dataset for Absolute Accuracy Evaluation in GNSS-Degraded Environments

Wei Zhang, Vincent Ress, David Skuddis, Uwe Soergel, Norbert Haala

Institute for Photogrammetry and Geoinformatics, University of Stuttgart, Germany - [firstname.lastname@ifp.uni-stuttgart.de](mailto:firstname.lastname@ifp.uni-stuttgart.de)

**Keywords:** SLAM, RTK-SLAM, Absolute accuracy evaluation, Georeferencing, Indoor-outdoor positioning, GNSS-denied environments, Geodetic ground truth

## Abstract

RTK-SLAM systems integrate simultaneous localization and mapping (SLAM) with real-time kinematic (RTK) GNSS positioning, promising both relative consistency and globally referenced coordinates for efficient georeferenced surveying. A critical and underappreciated issue is that the standard evaluation metric, Absolute Trajectory Error (ATE), first fits an optimal rigid-body transformation between the estimated trajectory and reference before computing errors. This so-called SE(3) alignment absorbs global drift and systematic errors, making trajectories appear more accurate than they are in practice, and is unsuitable for evaluating the global accuracy of RTK-SLAM. We present a geodetically referenced dataset and evaluation methodology that expose this gap. A key design principle is that the RTK receiver is used solely as a *system input*, while ground truth is established independently via a geodetic total station. This separation is absent from all existing datasets, where GNSS typically serves as (part of) the ground truth. The dataset is collected using a handheld RTK-SLAM device across two representative scenes, covering diverse GNSS conditions, including open-sky, building-obstructed areas, underpasses, outdoor-to-indoor transitions, and indoor environments. We evaluate LiDAR-inertial, visual-inertial, and LiDAR-visual-inertial RTK-SLAM systems alongside standalone RTK, reporting direct global accuracy and SE(3)-aligned relative accuracy to make the gap explicit. Results show that SE(3) alignment can underestimate absolute positioning error by up to 76%. RTK-SLAM achieves centimeter-level absolute accuracy in open-sky conditions and maintains decimeter-level global accuracy indoors, where standalone RTK degrades to tens of meters. The dataset, calibration files, and evaluation scripts are publicly available at <https://rtk-slam-dataset.github.io/>.

## 1. Introduction

Accurate and reliable positioning is fundamental for surveying, geospatial data acquisition, and robotic navigation. Conventional geodetic techniques achieve this by establishing observations within global coordinate frames using GNSS receivers and total stations. While these methods can deliver millimeter-level accuracy, they are typically tied to static instrument setups or point-by-point observations with a survey pole, which makes data collection labor-intensive and time-consuming, especially in large or complex environments. Simultaneous localization and mapping (SLAM) has emerged as a complementary approach that provides accurate relative positioning by continuously estimating the trajectory of a sensor platform while reconstructing the surrounding space (Cadena et al., 2016). SLAM operates effectively in GNSS-denied environments, such as urban canyons or indoor facilities, but its results remain confined to a local coordinate system. As a result, SLAM maps from different surveys cannot be directly integrated into geodetic or BIM coordinate frames without additional georeferencing effort.

Recent advances have led to the integration of SLAM with RTK GNSS positioning, often referred to as SLAM-RTK or RTK-SLAM systems (Shan et al., 2020, Wang et al., 2024). These hybrid solutions combine the global accuracy of GNSS positioning with the robustness of SLAM, offering two key advantages. First, they provide globally referenced coordinates even when operating across outdoor and indoor domains, with SLAM constraining drift when GNSS signals are degraded or unavailable. Second, they enable mobile and efficient surveying: instead of occupying each checkpoint individually, surveyors can simply walk through the environment with a handheld device, continuously recording georeferenced data. This

mobility lowers the barrier for large-scale and high-frequency surveys, making it attractive for construction monitoring, asset management, and rapid documentation tasks.

Despite this promise, important open questions remain. GNSS accuracy is strongly affected by multipath and obstruction (Yuan et al., 2023), and the degree to which SLAM can maintain global accuracy when GNSS signals degrade or are lost has not been rigorously quantified. More importantly, existing SLAM benchmarks evaluate accuracy with SE(3)-aligned ATE (Sturm et al., 2012), which fits a rigid transformation between the estimated and reference trajectories before computing errors. This alignment is appropriate when only relative accuracy matters, but it is fundamentally incompatible with evaluating absolute global positioning (see Section 4.2 for a detailed discussion). A trajectory that is meters away from its true global position can still yield a near-zero SE(3)-aligned ATE if its internal geometry is consistent. For RTK-SLAM systems intended for georeferenced surveying, this distinction is critical.

To address these gaps, we propose a dedicated dataset and evaluation methodology. The contributions are:

- **A geodetically referenced RTK-SLAM dataset** covering outdoor GNSS-degraded and indoor GNSS-denied environments, with RTK measurements used exclusively as system inputs, not as ground truth. Sub-centimeter ground truth is established independently via geodetic total station. To our knowledge, this is the first dataset enabling direct evaluation of absolute global RTK-SLAM accuracy across outdoor and indoor scenes with this separation.
- **An evaluation methodology** for absolute global accuracy without SE(3) alignment, applicable to any SLAM system

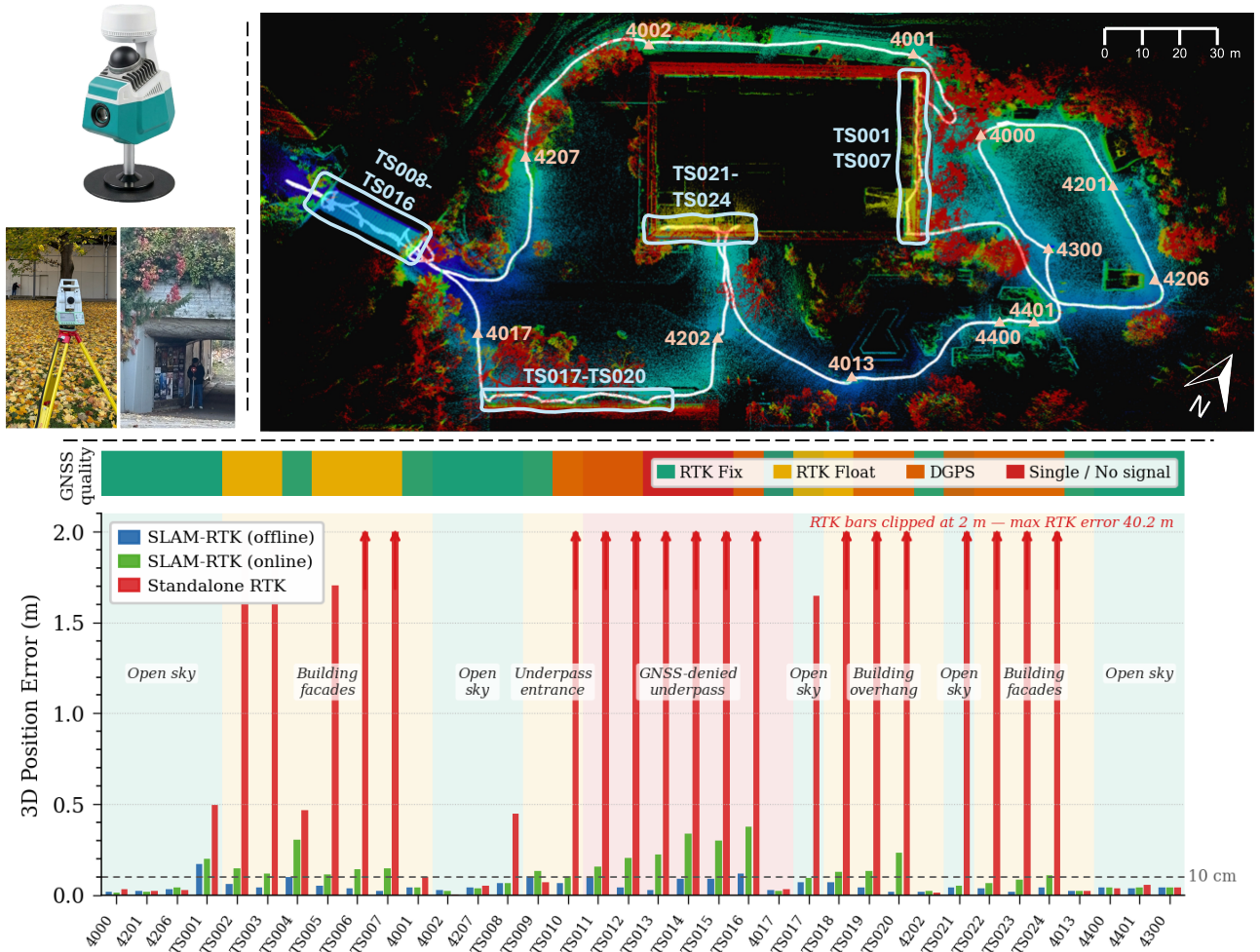


Figure 1. **Top:** Equipment setup (left) and overview of checkpoints overlaid on the SLAM map of the Stadtgarten scene (right). Orange marked checkpoints are under open sky, while cyan-marked checkpoints are under GNSS obstruction (e.g. buildings, trees, underpass). **Bottom:** Absolute 3D error per checkpoint for Stadtgarten Seq. 1 using FAST-LIO-SAM method. Standalone RTK errors grow to tens of meters in GNSS-degraded zones, while offline RTK-SLAM remains mostly below 10 cm.

that outputs globally referenced coordinates. Comparing against standard SE(3)-aligned ATE reveals that the alignment can underestimate absolute global errors by up to 76 %, masking critical failures.

- **Benchmarking of various RTK-SLAM systems** across scenes, reporting both online and offline results, with analysis of positioning drift in relation to GNSS outages. We show that while standalone RTK degrades to tens of meters, offline LiDAR-aided methods can maintain decimeter-level absolute accuracy in challenging GNSS-degraded conditions.

## 2. Related Work

### 2.1 LiDAR-Inertial and Visual-Inertial Odometry

LiDAR-based SLAM has advanced significantly in recent years. LOAM (Zhang and Singh, 2014) introduced edge and planar feature extraction for scan-to-map registration. LIO-SAM (Shan et al., 2020) extended this with a factor graph backend supporting IMU pre-integration and GNSS factors, enabling globally consistent mapping. FAST-LIO2 (Xu et al.,

2022) replaced feature extraction with direct point-to-map registration using an incremental k-d tree, achieving higher efficiency on solid-state LiDARs such as the Livox MID360. On the other hand, visual-inertial odometry (VIO) fuses camera and IMU measurements to estimate trajectory without LiDAR. Leutenegger et al. (Leutenegger et al., 2015) pioneered keyframe-based VIO using nonlinear optimization, demonstrating that tightly coupled camera-IMU factor graphs yield accurate and consistent state estimates. VINS-Mono (Qin et al., 2018) extended this with sliding-window optimization and loop closure for robust monocular operation. OKVIS2 (Leutenegger, 2022) scaled the keyframe-based formulation to multi-camera setups with real-time loop closure.

### 2.2 SLAM with GNSS Integration

Both LiDAR-inertial and visual-inertial systems can serve as odometry front-ends within a factor graph that additionally incorporates GNSS position factors, enabling globally referenced trajectory estimation. FAST-LIO-SAM (Wang, 2022) exemplifies this for LiDAR-inertial systems, combining the FAST-LIO2 front-end with the LIO-SAM graph optimization backend. For visual-inertial systems, VINS-Fusion (Qin et al., 2018, Qin et al., 2025) extends VINS-Mono with GNSS fusion and a general multi-sensor factor graph, enabling globally referenced tra-

Table 1. Comparison of representative SLAM and positioning datasets. *RTK role*: whether RTK is used as system input or ground truth. *Abs. geodetic*: absolute accuracy assessable without SE(3) alignment.  $\checkmark$  = yes,  $-$  = no,  $\sim$  = partial.

Dataset	Environment	Sensors	GT type	RTK role	GT accuracy	Abs. geodetic
KITTI (Geiger et al., 2013)	Urban roads	LiDAR, Cam, IMU, GNSS	RTK/INS	GT	<10 cm	$\sim$
EuRoC (Burri et al., 2016)	Indoor lab	Cam, IMU	Motion capture	-	<1 mm	-
MulRan (Kim et al., 2020)	Urban outdoor	LiDAR, Radar, IMU, GNSS	RTK/INS	GT	<10 cm	$\sim$
OpenLORIS (Shi et al., 2020)	Indoor scenes	LiDAR, RGB-D, Cam, IMU	Mocap / 2D LiDAR SLAM	-	<1 mm / 10 cm	-
Hilti-Oxford (Zhang et al., 2022)	Construction	LiDAR, Cam, IMU	Laser scanner	-	<1 mm	-
WHU-Helmet (Li et al., 2023)	Campus out/indoor	LiDAR, Cam, IMU, GNSS	FOG-IMU + PPK + LiDAR	GT	cm-level	$\sim$
MCD (Nguyen et al., 2024)	Multi-campus	LiDAR, Cam, IMU, UWB	LiDAR + Survey map	-	cm-level	-
M2DGR+ (Yin et al., 2024)	Campus out/indoor	LiDAR, Cam, IMU, GNSS	Mocap / RTK	GT	<1 mm / 2 cm	$\sim$
FPortV2 (Wei et al., 2025)	Campus + urban	LiDAR, Cam, IMU, GNSS	TS + RTK	GT	1 mm / 2 cm	$\sim$
<b>Ours</b>	<b>Park + construction</b>	<b>LiDAR, Cam, IMU, RTK</b>	<b>TS + static GNSS</b>	<b>Input</b>	<b>&lt;1 cm</b>	<b><math>\checkmark</math></b>

jectories. Lightweight systems combining GNSS with visual-inertial odometry for seamless indoor-outdoor navigation have also been proposed (Angelats et al., 2021). OKVIS2-X (Boche et al., 2025) takes this further with a configurable system supporting visual-inertial-GNSS (VIG) and LiDAR-visual-inertial-GNSS (LVIG) configurations within the same keyframe-based backend. Wang et al. (Wang et al., 2024) explore tighter GNSS-inertial-visual-LiDAR coupling. Despite these advances, these existing methods have not been evaluated in terms of direct global accuracy against geodetic ground truth.

### 2.3 SLAM Benchmarks and Datasets

A number of multi-sensor SLAM datasets have been proposed for benchmarking odometry and mapping systems. KITTI (Geiger et al., 2013) provides a large-scale outdoor benchmark, while EuRoC (Burri et al., 2016) targets visual-inertial odometry in indoor environments. The Hilti SLAM Challenge (Zhang et al., 2022) focuses on construction scenarios with handheld devices but evaluates only relative accuracy. MulRan (Kim et al., 2020) offers long-term outdoor sequences without geodetic ground truth. Recent datasets such as MCD (Nguyen et al., 2024), FusionPortableV2 (Wei et al., 2025), M2DGR+ (Yin et al., 2024), and WHU-Helmet (Li et al., 2023) expand sensor diversity and environments, yet none systematically evaluate absolute global accuracy of RTK-SLAM across outdoor and indoor scenes against independent geodetic references. Geodetic evaluation using total stations has been applied to UWB-based indoor positioning (Di Pietra et al., 2020), but not to mobile SLAM across mixed environments. Similarly, indoor mapping benchmarks (Wang et al., 2020) and handheld LiDAR SLAM comparisons (Trybała et al., 2023) lack globally referenced evaluation. Most benchmarks rely on SE(3)-aligned ATE (Sturm et al., 2012), which is unsuitable for assessing global accuracy. A key limitation is the role of GNSS: in existing datasets (e.g., KITTI, MulRan, M2DGR+, FusionPortableV2, WHU-Helmet), GNSS serves as (part of) the ground truth rather than an input modality, preventing meaningful assessment of how well GNSS-aided SLAM maintains absolute accuracy. In contrast, our dataset uses RTK strictly as system input, while ground truth is established independently via total station and static GNSS observations. Table 1 summarizes these distinctions across representative datasets.

### 3. Dataset

This section describes the dataset collected for this work. We first introduce the sensor platform and its calibration, then describe the two data collection scenes and the geodetic ground truth establishment procedure.

#### 3.1 Sensor Platform

Data acquisition was performed using a handheld RTK-SLAM device comprising a Livox MID360 LiDAR sensor with integrated IMU, a 2 megapixel global shutter camera, and a UM980 GNSS receiver. The Livox MID360 provides a  $360^\circ$  horizontal and  $59^\circ$  vertical field of view with a non-repetitive scan pattern, operating at 10 Hz. IMU measurements are recorded at 200 Hz. Differential GNSS corrections were provided by the German SAPOS service (Riecken and Kurtenbach, 2017), enabling the GNSS receiver to operate in RTK mode and achieve centimeter-level positioning accuracy under open-sky conditions.

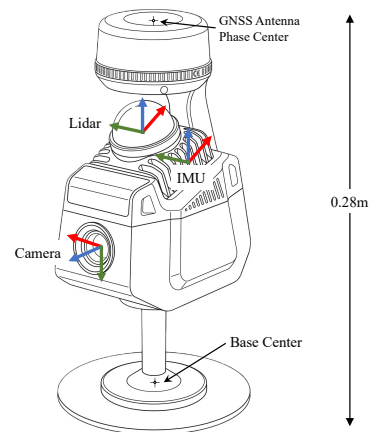


Figure 2. Sensor platform with coordinate frames (red =  $x$ , green =  $y$ , blue =  $z$ ) for LiDAR, IMU, and camera. GNSS antenna phase center (top) references RTK measurements. The base center (bottom) is matched against checkpoints.

Figure 2 illustrates the physical layout of the device and the individual coordinate frames of each sensor. The GNSS antenna phase center at the top of the device is the reference point for

RTK position measurements, while the base center at the bottom of the pole is the physical reference point matched against surveyed checkpoints. All inter-sensor rigid body transformations are expressed relative to the IMU frame. The dataset is released in ROS bag and EuRoC format. To comply with privacy requirements, all camera images were anonymized prior to release by blurring human faces using *deface* (ORB-HD, 2026).

### 3.2 Sensor Calibration

Table 2. Sensor calibration parameters.

Parameter	Value	Method
<i>Camera intrinsics (1600 × 1200 px)</i>		
$f_x, f_y$ (px)	890.60, 890.62	OpenCV checkerboard
$c_x, c_y$ (px)	780.97, 589.79	OpenCV checkerboard
$k_1, k_2$	-0.1471, 0.0810	OpenCV checkerboard
$p_1, p_2$	$-3.94 \times 10^{-4}, 6.56 \times 10^{-4}$	OpenCV checkerboard
<i>Camera → IMU extrinsic <math>\mathbf{T}_{C \rightarrow I}</math></i>		
Rotation (r/p/y, deg)	0.21, 67.44, -89.84	Kalibr
Translation (m)	(0.022, -0.048, -0.058)	Kalibr
Time offset (s)	-0.0206 (camera delay)	Kalibr
<i>LiDAR → IMU extrinsic <math>\mathbf{T}_{L \rightarrow I}</math></i>		
Rotation	identity	Livox MID360 manual
Translation (m)	(-0.011, -0.023, 0.044)	Livox MID360 manual
<i>Reference point offsets from IMU (m)</i>		
GNSS antenna phase center	(0.023, -0.023, 0.090)	CAD model
Base center	(-0.073, -0.023, -0.172)	CAD model

Accurate extrinsic calibration and precise time synchronization are critical prerequisites for high-accuracy multi-sensor fusion, as uncompensated spatial offsets or temporal misalignment directly degrade positioning accuracy. Table 2 summarizes the intrinsic and extrinsic parameters for all sensors. Camera intrinsics were obtained using the checkerboard method (Zhang, 2000) in OpenCV with a 400 mm × 600 mm target. Camera-to-IMU extrinsics and the temporal offset were jointly estimated using Kalibr (Furgale et al., 2013) with the same target and sufficient IMU excitation. LiDAR-to-IMU extrinsics are adopted from the device user manual. The offsets of the GNSS antenna phase center and the base center relative to the IMU frame were derived from the CAD model. The LiDAR and its built-in IMU are hardware-synchronized to GNSS time via a 1 PPS signal from the GNSS receiver. The camera is triggered by the SoC with a -20.6 ms delay relative to the IMU, as estimated by Kalibr.

Table 3. Dataset overview. The dataset comprises two scenes with four sequences in total.

Sequence	Duration	Length	RTK Fix[%]	Ctrl. Pts	Type
Stadtgarten 1	26 min 42 s	1.04 km	54	36	Outdoor park
Stadtgarten 2	14 min 36 s	0.46 km	40	19	Outdoor park
Constr. Hall 1	12 min 21 s	0.48 km	25	16	Out.+Indoor
Constr. Hall 2	9 min 59 s	0.39 km	23	16	Out.+Indoor

### 3.3 Stadtgarten Scene

The Stadtgarten scene was collected in Stuttgart Stadtgarten, a public park with diverse GNSS visibility conditions. The operator walked through the environment at normal walking pace and held the device stationary over the checkpoints. Two sequences were captured covering the same area. Geodetic checkpoints are distributed across three distinct zones: open-sky areas, partially obstructed areas under tree cover or near building facades, and a GNSS-denied 30 m-long underpass tunnel. As shown in Figure 3, the tunnel interior is dark and has a highly symmetric cross-sectional geometry, which can cause LiDAR odometry to degenerate along the tunnel axis and makes



Figure 3. Example camera images overlaid with projected LiDAR points, colored by depth. **Top:** Stadtgarten scene near building (left) and the GNSS-denied underpass tunnel (right). **Bottom:** Construction Hall scene entrance area (left) and the indoor construction hall (right).

this segment particularly challenging. Figure 1 (top) illustrates the spatial distribution of the checkpoints.

### 3.4 Construction Hall Scene

The Construction Hall scene was collected at a large construction site (IntCDC, University of Stuttgart)<sup>1</sup>. Two sequences were captured, each beginning and ending outdoors with good GNSS visibility and RTK fix, and traversing the interior of the construction hall where GNSS signals are severely degraded, with only weak receptions likely due to skylights or multipath reflections. The sequences cover the same area but with clockwise and counter-clockwise walking directions, providing complementary views of the outdoor-to-indoor transition. Table 3 summarizes the statistics of the recorded sequences and Figure 3 shows representative camera images from the scene.

### 3.5 Geodetic Ground Truth

Accurate geodetic ground truth is a central contribution of this dataset, as it enables direct evaluation of absolute global positioning accuracy without reliance on SE(3) alignment. For both scenes, ground truth was established using a two-stage procedure. First, a set of open-sky anchor points was surveyed via static GNSS observations, achieving a position standard deviation of <5 mm. A Leica TS16 total station was then oriented to these anchors and used to measure the remaining checkpoints via reflective prisms. These measurements covered points under GNSS obstruction or inside GNSS-denied areas, carrying the global reference frame into regions where kinematic GNSS is unavailable. For the Construction Hall scene, an additional instrument setup was required to reach the deeper indoor checkpoints. The survey was extended via a further traverse, where a second total station setup was established inside the building by resection onto targets measured from the outdoor station. This propagated the global reference frame through the full outdoor-to-indoor transition. The resulting ground truth covers both outdoor and indoor checkpoints with an estimated accuracy of better than 1 cm. During data collection, the handheld device was carefully centered over these checkpoints and held stationary,

<sup>1</sup> <https://www.intcdc.uni-stuttgart.de/research/research-infrastructure/>

enabling direct comparison between the estimated positions and the surveyed coordinates.

### 3.6 Terminology

Throughout this paper, *GNSS* refers to the satellite navigation systems in general (GPS, Galileo, GLONASS, and BeiDou). *RTK* refers specifically to the differential positioning mode in which the receiver resolves carrier-phase integer ambiguities using base-station corrections, achieving centimeter-level accuracy. When satellite signals or SAPOS corrections are unavailable or insufficient, the receiver falls back to RTK float, DGPS, or single-point positioning in order of decreasing accuracy. All of these modes are GNSS-based but not RTK-grade. We use “GNSS-denied” and “GNSS-degraded” to describe signal availability conditions, and “GNSS quality” or “GNSS status” to describe the positioning mode of the receiver. The surveyed reference points are called *checkpoints* throughout this paper. In photogrammetric practice, ground control points (GCPs) are used to actively constrain a map during processing, whereas checkpoints are used solely to verify the accuracy of the final result. Since our surveyed points play no role in the estimation pipeline and serve purely as an independent accuracy reference, the term checkpoint is used.

## 4. Experiments

We first introduce the evaluated RTK-SLAM methods and the evaluation metrics, then present per-scene results for all four sequences, and conclude with a cross-cutting discussion of the key findings.

### 4.1 Evaluated Methods

**FAST-LIO-SAM.** FAST-LIO-SAM (Wang, 2022) couples the FAST-LIO2 (Xu et al., 2022) LiDAR-inertial odometry front-end with the factor graph backend of LIO-SAM (Shan et al., 2020), with RTK measurements incorporated as loose-coupling GNSS position factors. We refer the reader to the respective papers for implementation details. For evaluation we report two types of results. *Online* poses are estimated causally without access to future measurements. *Offline* results are obtained by applying global pose graph optimization over the complete trajectory. The offline result is expected to yield higher accuracy, as batch optimization can propagate GNSS corrections across GNSS-denied sections in both directions.

**OKVIS2-X.** OKVIS2-X (Boche et al., 2025) is a keyframe-based SLAM system with tightly coupled GNSS integration, supporting flexible sensor modality combinations within a unified factor graph. GNSS measurements are fused directly with visual reprojection and inertial factors by explicitly estimating a 4-DoF transformation  $\mathbf{T}_{GW}$  that aligns the local SLAM frame with the global reference frame. We evaluate two configurations: **OKVIS2-X(lvig)** uses the full LiDAR-visual-inertial-GNSS modality set, while **OKVIS2-X(vig)** relies on visual-inertial-GNSS only. Both output a globally referenced trajectory for direct comparison with geodetic checkpoints, and the two configurations also serve as an ablation to quantify the contribution of LiDAR depth in GNSS-degraded conditions.

### 4.2 Evaluation Protocol

**Coordinate transformation pipeline.** RTK-SLAM methods estimate poses in a local east-north-up (ENU) Cartesian frame

whose origin is fixed at the first valid RTK fix. Poses are expressed in the IMU body frame  $I$ . To compare against surveyed checkpoints, we first compute the 3D position of the device base center  $B$  in the ENU world frame:

$$\mathbf{p}_{W,B}^{(k)} = \mathbf{p}_{W,I}^{(k)} + \mathbf{R}_{W,I}^{(k)} \mathbf{t}_{I \rightarrow B}, \quad (1)$$

where  $\mathbf{p}_{W,I}^{(k)}$  and  $\mathbf{R}_{W,I}^{(k)}$  are the estimated position and orientation at timestep  $k$  in the IMU body frame, and  $\mathbf{t}_{I \rightarrow B}$  is the fixed offset from the IMU origin to the base center expressed in the IMU body frame (see Table 2). Since we focus on evaluating the positioning error, this reduces to position only. The resulting ENU position  $\mathbf{p}_{W,B}^{(k)} = (e, n, u)^\top$  of the base center is then converted to geographic coordinates  $(\varphi, \lambda, h)$ . The ENU origin is the geodetic coordinates  $(\varphi_0, \lambda_0, h_0)$  of the first valid RTK fix. Finally,  $(\varphi, \lambda, h)$  is projected to UTM Zone 32U, all within the ETRS89 reference frame, which is the native coordinate system of the SAPOS correction service. The resulting easting, northing, and height  $(\hat{E}_i, \hat{N}_i, \hat{h}_i)$  can be compared directly to the surveyed checkpoint coordinates  $(E_i^*, N_i^*, h_i^*)$ .

**Absolute accuracy metric.** Let  $\boldsymbol{\varepsilon}_i = (\hat{E}_i - E_i^*, \hat{N}_i - N_i^*, \hat{h}_i - h_i^*)^\top$  denote the 3D position error at checkpoint  $i$ . The root-mean-square error over  $N$  checkpoints is

$$\text{RMSE} = \sqrt{\frac{1}{N} \sum_{i=1}^N \|\boldsymbol{\varepsilon}_i\|^2}. \quad (2)$$

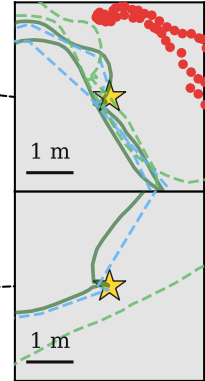
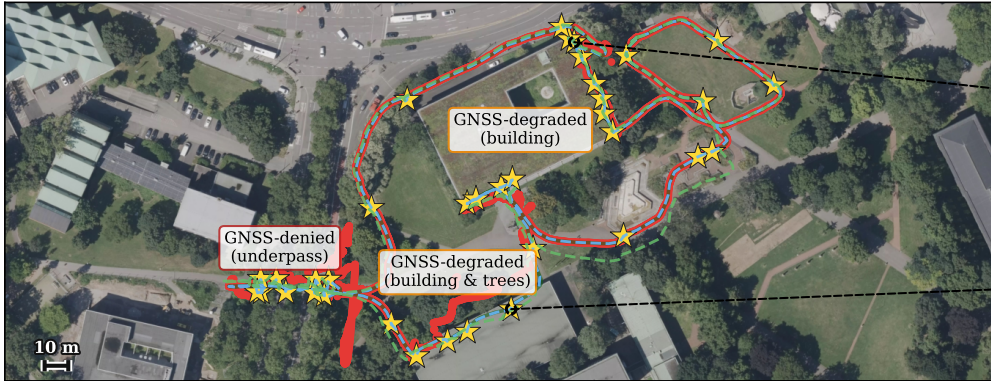
This metric is a direct adaptation of the Absolute Trajectory Error (ATE) (Sturm et al., 2012) to a globally referenced setting. The key difference from standard ATE is that no SE(3) alignment is applied. Since the estimated trajectory already resides in the target geodetic coordinate frame after the transformation described above, both global offset and accumulated drift can be reflected in the error. The timestamp of each checkpoint visit is pre-determined by detecting the stationary periods in the SLAM trajectory and matching them to the surveyed checkpoint locations. The resulting lookup table is then shared across all evaluated methods to ensure a consistent and reproducible evaluation.

**SE(3)-aligned relative accuracy and the gap to absolute accuracy.** To make the distinction between global and relative accuracy, we additionally compute for each method the SE(3)-aligned ATE. Given matched position pairs  $\{(\hat{\mathbf{p}}_i, \mathbf{p}_i^*)\}$ , we find the optimal rigid transformation

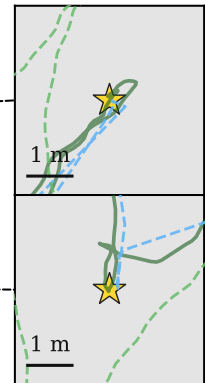
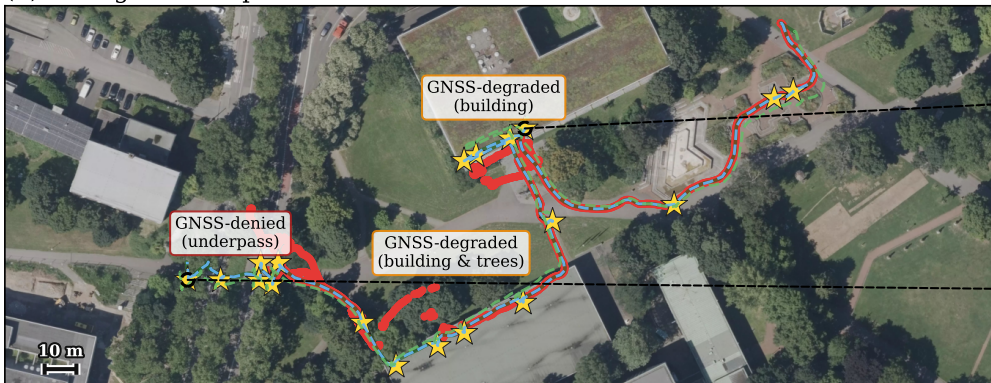
$$(\mathbf{R}^*, \mathbf{t}^*) = \arg \min_{R \in \text{SO}(3), \mathbf{t}} \sum_{i=1}^N \|\mathbf{R} \hat{\mathbf{p}}_i + \mathbf{t} - \mathbf{p}_i^*\|^2 \quad (3)$$

and report the RMSE of the residuals  $\|\mathbf{R}^* \hat{\mathbf{p}}_i + \mathbf{t}^* - \mathbf{p}_i^*\|$ . This is equivalent to the standard ATE used in SLAM benchmarking (Sturm et al., 2012). The alignment absorbs any constant systematic offset and global orientation error between the estimated and reference frame. The difference between the global absolute RMSE (Eq. 2) and the SE(3)-aligned RMSE therefore quantifies how much of the absolute error is hidden by this alignment. For a RTK-SLAM system that successfully maintains global accuracy, these two values should be nearly the same. A large gap indicates that the system has significant global drift or systematic errors that the standard metric would miss.

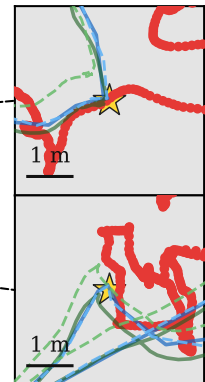
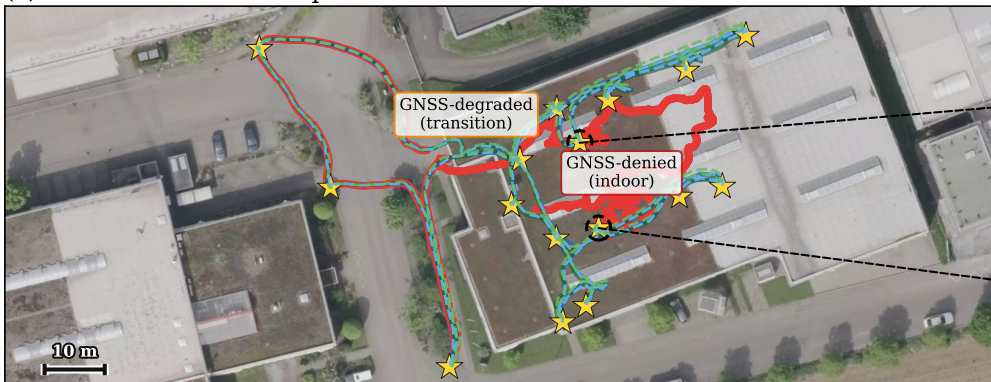
(a) Stadtgarten Seq. 1



(b) Stadtgarten Seq. 2



(c) Construction Hall Seq. 1



(d) Construction Hall Seq. 2

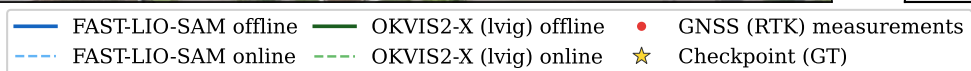
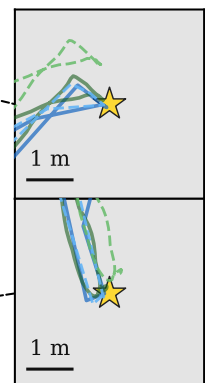
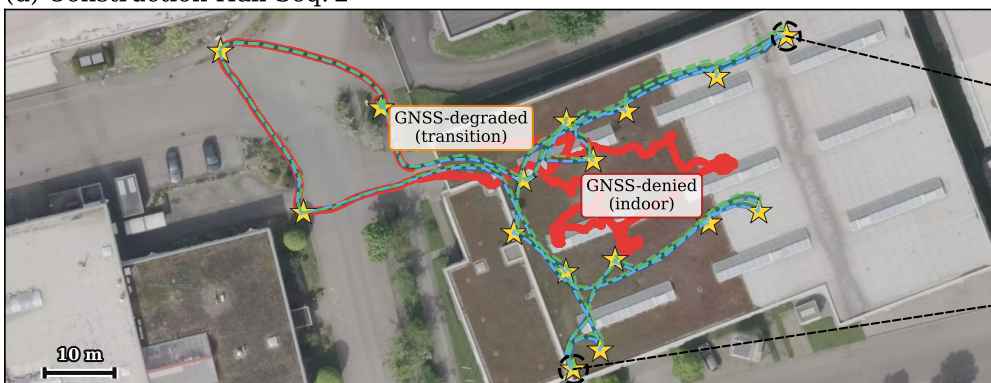


Figure 4. Trajectory comparisons for all four sequences on satellite imagery. Rows (a)–(b): Stadtgarten Seq. 1–2; rows (c)–(d): Construction Hall Seq. 1–2. GNSS-degraded zones are annotated. In the Construction Hall indoor environment, the GNSS receiver still obtains occasional measurements, but only at single-point positioning accuracy.

Table 4. Quantitative accuracy results across all sequences and methods. We report absolute ATE for both online and offline results, as well as relative accuracy of the offline results after SE(3) alignment. Gap [%] denotes the alignment-induced error reduction, revealing hidden systematic offsets or orientation errors. The best absolute ATE are marked in bold for each sequence.

Scene	Seq.	FAST-LIO-SAM				OKVIS2-X(vig)				OKVIS2-X(lvig)				RTK Standalone [m]
		Online [m]	Offline [m]	SE3 [m]	Gap [%]	Online [m]	Offline [m]	SE3 [m]	Gap [%]	Online [m]	Offline [m]	SE3 [m]	Gap [%]	
Stadtgarten	Seq. 1	0.162	<b>0.068</b>	0.065	4	3.276	0.189	0.185	2	4.103	<b>0.068</b>	0.060	12	13.98
Stadtgarten	Seq. 2	0.150	0.099	0.077	22	2.695	0.907	0.831	8	3.180	<b>0.092</b>	0.080	13	11.99
Constr. Hall	Seq. 1	0.256	<b>0.248</b>	0.220	11	1.437	0.788	0.579	27	0.761	0.321	0.227	29	12.01
Constr. Hall	Seq. 2	0.439	0.373	0.089	76	3.715	0.700	0.511	27	0.825	<b>0.170</b>	0.081	52	14.84

### 4.3 Results and Discussion

We show the per-point errors and trajectories for all four sequences in Figure 1 (bottom) and Figure 4, with quantitative results summarised in Table 4. Three distinct error regimes emerge as GNSS availability degrades. In open-sky zones, all RTK-SLAM methods achieve sub-5 cm absolute accuracy. As GNSS degrades near building facades and trees, standalone RTK errors grow to several meters, while LiDAR-aided RTK-SLAM methods remain mostly within 10 cm. In fully GNSS-denied zones, standalone RTK errors reach 10–40 m, while the offline results of FAST-LIO-SAM and OKVIS2-X(lvig) maintain decimeter level accuracy by relying on LiDAR-inertial odometry to bridge the outage. The Construction Hall sequences represent a more challenging scenario. The GNSS-denied interior spans over 400 s and 150 m of travel, with only short outdoor segments at the start and end. Compared to Stadtgarten, absolute errors are substantially larger even in offline results, directly reflecting the longer GNSS outage.

**Online vs. Offline Estimation** Online results accumulate larger errors during GNSS outages, confirming the benefit of offline global optimization with entire observations, which propagates corrections both forward and backward in time. For the online results, especially for OKVIS2-X, significantly larger errors are observed. A possible cause is its global reference frame initialization strategy. It fixes the global orientation once the yaw uncertainty of the estimated 4-DoF world-to-global transformation falls below a fixed threshold ( $0.1^\circ$ ), which prevents further refinement when additional RTK fixes become available. In comparison, FAST-LIO-SAM continuously performs global batch optimization directly in the global frame.

**LiDAR-aided vs. Vision-only** Both LiDAR-aided methods achieve comparable absolute ATE of <10 cm in Stadtgarten. Without LiDAR, OKVIS2-X(vig) achieves 18.9 cm in Seq. 1 but degrades severely in Seq. 2 (90.7 cm) due to front-end divergence in the texture-poor underpass that LiDAR depth would otherwise prevent. In Construction Hall, OKVIS2-X(vig) performs substantially worse in absolute terms. Without direct LiDAR geometric observations to constrain the trajectory during the indoor section, visual-inertial drift accumulates more rapidly, and GNSS re-acquisition upon exiting the building can only partially recover the global position.

**Absolute vs. Relative Accuracy** The alignment gap in Stadtgarten is small for all methods (2–22 %), indicating that RTK effectively anchors the trajectories globally in this predominantly open-sky scene. In Construction Hall, gaps reach up to 76 %, suggesting that the brief outdoor sections with RTK fix are insufficient to precisely anchor the global coordinate frame. Beyond positional drift, a global systematic error can

accumulate during the indoor traversal that SE(3) alignment absorbs but geodetic evaluation exposes.

Table 5. Comparison of SLAM-only relative ATE vs. RTK-SLAM relative and absolute ATE.

Seq.	SLAM-only Rel. [cm]	RTK-SLAM Rel. [cm]	RTK-SLAM Abs. [cm]
Stadtgarten 1	61.5	<b>6.5</b>	6.8
Stadtgarten 2	26.4	<b>7.7</b>	9.9
Construction 1	31.4	<b>22.0</b>	24.8
Construction 2	12.2	<b>8.9</b>	37.3

**SLAM-only vs. RTK-SLAM** Beyond providing a global coordinate reference, we analyze whether RTK integration can also improve relative trajectory accuracy. To quantify this, we evaluate the FAST-LIO-SAM result without RTK as a measure of SLAM-only relative accuracy, and compare it against its RTK-SLAM offline results in Table 5. In both scenes, the relative accuracy of SLAM-only is worse than that of RTK-SLAM, indicating the positive impact of RTK integration in correcting long-range odometry drift, particularly in sequences without loop closure opportunities.

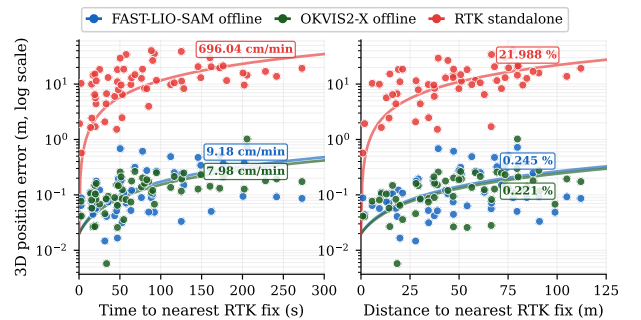


Figure 5. 3D absolute positioning error (log scale) as a function of time (left) and distance (right) to the nearest RTK fix, aggregated over the measurements from all sequences.

Regression lines indicate the average drift rate.

**Drift Behavior Under GNSS Outage** We focus this analysis on the offline results, which represent the best accuracy from each system. Figure 5 shows how absolute error grows with GNSS outage duration and travel distance. Because offline optimization propagates RTK corrections both forward and backward, the x-axis is the distance to the nearest RTK fix, rather than only since the last fix. The y-axis is shown on a logarithmic scale to visualize the wide error range across methods. A linear drift model  $\epsilon(x) = \epsilon_0 + \alpha x$  is fitted with the intercept fixed at  $\epsilon_0 = 2$  cm, representing the standard error of a typical

RTK fix measurement. The slope  $\alpha$  captures the drift that accumulates during the outage. A clear positive correlation can be observed across all methods, confirming that error grows steadily with proximity to RTK coverage. The key observation is that RTK-SLAM methods maintain effective position tracking even as GNSS quality degrades. The fitted drift rates are low: 9.2 cm/min (0.25 % of path length) for FAST-LIO-SAM and 8.0 cm/min (0.22 %) for OKVIS2-X(lvig), reflecting the effectiveness of LiDAR odometry in bounding dead-reckoning drift during GNSS outages. In contrast, standalone RTK degrades significantly once signal quality deteriorates. These drift rates can explain the absolute ATE results of the Construction Hall sequences.

## 5. Conclusion

We have presented a RTK-SLAM dataset and evaluation methodology that together address a critical gap in the field. The dataset provides synchronized LiDAR, camera, IMU, and RTK inputs alongside geodetic ground truth established independently via total station and static GNSS, enabling direct evaluation of absolute global positioning accuracy. To complement the dataset, we propose an evaluation protocol based on direct global accuracy metrics, explicitly addressing the limitation of SE(3)-aligned ATE, which absorbs global drift and can underestimate absolute errors by up to 76%. We evaluate different sensor-fusion configurations and observe that LiDAR-aided systems achieve consistently higher absolute accuracy, and offline results obtained through global optimization outperform online estimates, suggesting that surveyors can meaningfully improve output quality with a post-processing step. When GNSS degrades, standalone RTK deteriorates rapidly to meter-level errors, whereas RTK-SLAM methods maintain decimeter-level absolute accuracy even through GNSS-denied indoor environments. Future work will investigate tight fusion of raw GNSS measurements into the RTK-SLAM estimator, which we expect to further improve global accuracy during GNSS-degraded transitions.

## 6. Acknowledgements

Supported by the Deutsche Forschungsgemeinschaft (DFG, German Research Foundation) under Germany's Excellence Strategy – EXC 2120/1 – 390831618.

## References

- Angelats, E., Espín-López, P. F., Navarro, J. A., Parés, M. E., 2021. Performance Analysis of the IOPEs Seamless Indoor-Outdoor Positioning Approach. *Int. Arch. Photogramm. Remote Sens. Spatial Inf. Sci.*, XLIII-B4-2021, 229–235.
- Boche, S., Jung, J., Laina, S. B., Leutenegger, S., 2025. OKVIS2-X: Open keyframe-based visual-inertial SLAM configurable with dense depth or LiDAR, and GNSS. *IEEE Transactions on Robotics*.
- Burri, M., Nikolic, J., Gohl, P., Schneider, T., Rehder, J., Omari, S., Achtelik, M. W., Siegwart, R., 2016. The EuRoC micro aerial vehicle datasets. *The International Journal of Robotics Research*, 35(10), 1157–1163.
- Cadena, C., Carlone, L., Carrillo, H., Latif, Y., Scaramuzza, D., Neira, J., Reid, I., Leonard, J. J., 2016. Past, Present, and Future of Simultaneous Localization and Mapping: Toward the Robust-Perception Age. *IEEE Transactions on Robotics*, 32(6), 1309–1332.
- Di Pietra, V., Grasso, N., Piras, M., Dabove, P., 2020. Characterization of a Mobile Mapping System for Seamless Navigation. *Int. Arch. Photogramm. Remote Sens. Spatial Inf. Sci.*, XLIII-B1-2020, 227–234.
- Furgale, P., Rehder, J., Siegwart, R., 2013. Unified temporal and spatial calibration for multi-sensor systems. *2013 IEEE/RSJ International Conference on Intelligent Robots and Systems (IROS)*, IEEE, 1280–1286.
- Geiger, A., Lenz, P., Stiller, C., Urtasun, R., 2013. Vision meets robotics: The kitti dataset. *The international journal of robotics research*, 32(11), 1231–1237.
- Kim, G., Park, Y. S., Cho, Y., Jeong, J., Kim, A., 2020. Mulran: Multimodal range dataset for urban place recognition. *2020 IEEE International Conference on Robotics and Automation (ICRA)*, IEEE, 6246–6253.
- Leutenegger, S., 2022. OKVIS2: Realtime Scalable Visual-Inertial SLAM with Loop Closure. *arXiv preprint arXiv:2202.09199*.
- Leutenegger, S., Lynen, S., Bosse, M., Siegwart, R., Furgale, P., 2015. Keyframe-based visual-inertial odometry using non-linear optimization. *The International Journal of Robotics Research*, 34(3), 314–334.
- Li, Z., Cao, S., Fu, Y., Li, B., Zhang, Y., Ji, S., Yang, B., 2023. WHU-Helmet: A Helmet-Based Multisensor SLAM Dataset for the Evaluation of Real-Time 3D Mapping in Large-Scale GNSS-Denied Environments. *IEEE Transactions on Geoscience and Remote Sensing*, 61, 1–16.
- Nguyen, T.-M., Yuan, S., Nguyen, T. H., Yin, P., Cao, H., Xie, L., Wozniak, M., Jensfelt, P., Thiel, M., Ziegenbein, J. et al., 2024. Mcd: Diverse large-scale multi-campus dataset for robot perception. *Proceedings of the IEEE/CVF Conference on Computer Vision and Pattern Recognition*, 22304–22313.
- ORB-HD, 2026. deface: Video anonymization by face detection. GitHub repository.
- Qin, T., Cao, S., Pan, J., Shen, S., 2025. A General Optimisation-Based Framework for Global Pose Estimation With Multiple Sensors. *IET Cyber-Systems and Robotics*, 7(1), e70023.
- Qin, T., Li, P., Shen, S., 2018. VINS-Mono: A Robust and Versatile Monocular Visual-Inertial State Estimator. *IEEE Transactions on Robotics*, 34(4), 1004–1020.
- Riecken, J., Kurtenbach, E., 2017. Der Satellitenpositionierungsdienst der deutschen Landesvermessung—SAPOS®. *ZfV-Zeitschrift Für Geodäsie, Geoinformation und Landmanagement*.
- Shan, T., Englot, B., Meyers, D., Wang, W., Ratti, C., Rus, D., 2020. Lio-sam: Tightly-coupled lidar inertial odometry via smoothing and mapping. *2020 IEEE/RSJ international conference on intelligent robots and systems (IROS)*, IEEE, 5135–5142.

Shi, X., Li, D., Zhao, P., Tian, Q., Tian, Y., Long, Q., Zhu, C., Song, J., Qiao, F., Song, L. et al., 2020. Are we ready for service robots? The OpenLORIS-Scene datasets for lifelong SLAM. *2020 IEEE International Conference on Robotics and Automation (ICRA)*, IEEE, 3139–3145.

Sturm, J., Engelhard, N., Endres, F., Burgard, W., Cremers, D., 2012. A benchmark for the evaluation of RGB-D SLAM systems. *Proceedings of the IEEE/RSJ International Conference on Intelligent Robots and Systems (IROS)*, IEEE, 573–580.

Trybała, P., Kasza, D., Wajs, J., Remondino, F., 2023. Comparison of Low-Cost Handheld LiDAR-Based SLAM Systems for Mapping Underground Tunnels. *Int. Arch. Photogramm. Remote Sens. Spatial Inf. Sci.*, XLVIII-1/W1-2023, 517–524.

Wang, C., Dai, Y., El-Sheimy, N., Wen, C., Retscher, G., Kang, Z., Lingua, A., 2020. ISPRS Benchmark on Multisensory Indoor Mapping and Positioning. *ISPRS Ann. Photogramm. Remote Sens. Spatial Inf. Sci.*, V-5-2020, 117–123.

Wang, J., 2022. Fast-lio-sam: Fast-lio with smoothing and mapping. [https://github.com/kahowang/FAST\\_LIO\\_SAM](https://github.com/kahowang/FAST_LIO_SAM).

Wang, X., Li, X., Yu, H., Chang, H., Zhou, Y., Li, S., 2024. GIVL-SLAM: a robust and high-precision SLAM system by tightly coupled GNSS RTK, inertial, vision, and LiDAR. *IEEE/ASME Transactions on Mechatronics*, 30(2), 1212–1223.

Wei, H., Jiao, J., Hu, X., Yu, J., Xie, X., Wu, J., Zhu, Y., Liu, Y., Wang, L., Liu, M., 2025. FusionPortableV2: A unified multi-sensor dataset for generalized SLAM across diverse platforms and scalable environments. *The International Journal of Robotics Research*, 44(7), 1093–1116.

Xu, W., Cai, Y., He, D., Lin, J., Zhang, F., 2022. Fast-lio2: Fast direct lidar-inertial odometry. *IEEE Transactions on Robotics*, 38(4), 2053–2073.

Yin, J., Li, A., Xi, W., Yu, W., Zou, D., 2024. Ground-fusion: A low-cost ground slam system robust to corner cases. *2024 IEEE International Conference on Robotics and Automation (ICRA)*, 8603–8609.

Yuan, H., Zhang, Z., He, X., Dong, Y., Zeng, J., Li, B., 2023. Multipath mitigation in GNSS precise point positioning using multipath hierarchy for changing environments. *GPS Solutions*, 27(4), 193.

Zhang, J., Singh, S., 2014. Loam: Lidar odometry and mapping in real-time. *Proceedings of Robotics: Science and Systems (RSS)*.

Zhang, L., Helmberger, M., Fu, L. F. T., Wisth, D., Camurri, M., Scaramuzza, D., Fallon, M., 2022. Hilti-oxford dataset: A millimeter-accurate benchmark for simultaneous localization and mapping. *IEEE Robotics and Automation Letters*, 8(1), 408–415.

Zhang, Z., 2000. A flexible new technique for camera calibration. *IEEE Transactions on Pattern Analysis and Machine Intelligence*, 22(11), 1330–1334.